Crystalline Structures, Melting, and Crystallization of Linear Polyethylene in Cylindrical Nanopores

Kyusoon Shin,*,† Euntaek Woo,† Young Gyu Jeong,‡ Chulkyu Kim,† June Huh,§ and Kwang-Woo Kim⊥

School of Chemical and Biological Engineering, Seoul National University, Seoul 151-742, Republic of Korea; School of Advanced Materials and Systems Engineering, Kumoh National Institute of Technology, Gumi 730-701, Republic of Korea; Hyperstructured Organic Materials Research Center and School of Materials Science and Engineering, Seoul National University, Seoul 151-742, Republic of Korea; and Pohang Accelerator Laboratory, Pohang 790-784, Republic of Korea

Received May 1, 2007; Revised Manuscript Received July 7, 2007

ABSTRACT: The crystalline structures associated with melting and crystallization behaviors of monodisperse linear polyethylene confined in cylindrical nanopores were investigated by X-ray diffraction and differential scanning calorimetry. The crystalline structures, melting, and crystallization behaviors of PE under the imposed cylindrical confinement were noticeably different from those of the bulk state. The isothermal crystallization experiments showed that the overall crystallization of polyethylene in cylindrical nanopores was dominated by the nucleation rather than the growth of crystallites. The *c*- and *a*-axes of orthorhombic PE crystals developed in nanoporous alumina were preferentially oriented perpendicular to the long axis of cylindrical nanopore while the *b*-axis was parallel to the pore axis. The melting temperature of polyethylene in the nanopores was substantially depressed, and it was analyzed with the Thomson−Gibbs equation. The crystallinity of linear polyethylene in cylindrical nanopores was less than 50%, whereas the bulk value was 71.6%.

Introduction

During the past few decades, the physical behaviors of polymers under nanoscopic confinements have been of great scientific interest.[1−6] Relaxation of amorphous polymers[1−4] or block copolymer structures[6] within nanoscopically constrained environments are typical examples exhibiting nonclassical equilibrium properties. The investigation of polymer crystallization behavior under nanoscopic confinements is another important area in polymer physics due to the potential applications as well as scientific interest.

There have been several different approaches to investigate the crystallization under constrained environments.[7−24] Ultrathin films of semicrystalline polymers have been one of the preferred systems for studying the polymer crystallization under nanoscopic confinements due to their applications in fabricating the microelectronic systems.[7] Thin films are one dimensionally confined system which has one (supported by substrates) or two (freely standing) free surfaces. Frank and co-workers[7,9,10] have reported an extensive reduction of the crystallinity and the crystallization rate of ultrathin poly(di-*n*-hexylsilane) films (<50 nm in thickness).[9] They also showed that the crystallization behavior of ultrathin poly(di-*n*-hexylsilane) films on an octadecyltrichlorosilane-treated quartz surface was faster than on glass substrates because of the attractive interfacial interaction between the polymer and substrate.[10]

Crystalline−amorphous diblock copolymers have recently been widely studied.[11−20] In this system, the crystallizable components crystallize within the microdomains of diblock copolymers such as lamellae, double gyroid, cylinders, and spheres in order of 10 nm below their order−disorder transition temperatures (T_{ODT}).[25] Loo et al. have reported that the crystallization of polyethylene (PE) blocks within the microdomains of the diblock copolymers followed first-order kinetics (Avrami exponent, $n = 1$) in contrast with the sigmoidal crystallization kinetics in the bulk state.[14−16] This is because the crystallization of PE within the spherical microdomains of PE blocks was dominated by the homogeneous nucleation rather than the growth of crystallites. Cheng and co-workers have studied the orientation of polymer crystallites within the microdomains of diblock copolymers.[17−19] They have reported that the crystal orientation of poly(ethylene oxide) (PEO) was altered with the crystallization temperature[17] or the confinement dimension[18] in lamellar domains of poly(ethylene oxide)-*b*-polystyrene diblock copolymer systems due to the effect of geometric confinement on the crystallite growth. The orientation of crystals developed in the cylindrical microdomains was also found to be changed.[19]

Inorganic materials were used as nanoscopic templates, too. When crystalline polymers were blended with clay[21] or silicate gel,[22,23] the crystallinity and melting temperature of polymers were reduced with increasing the amount of inorganic components due to the disruption of the growth of polymer crystals. Steinhart et al. have shown that, in electrochemically fabricated porous materials, the curvature of the confinements can affect the crystal orientation of polymers.[24] By studying the orientation of crystals of poly(vinylidene fluoride) under cylindrical confinements, they have observed that the crystallites grow preferentially in the direction of minimum curvature on the surfaces of cylindrical confinements. The study on the crystallization behavior of ferroelectric or ferromagnetic materials such as poly(vinylidene fluoride) or cobalt under nanoscopic cylindrical confinement is particularly important for the fabrication of high-density storage device because densely packed nanorods have high density and strong electronic or magnetic properties

* To whom correspondence should be addressed: Tel +82-2-8809386, Fax +82-2-8847355, e-mail shin@snu.ac.kr.

† School of Chemical and Biological Engineering, Seoul National University.

‡ Kumoh National Institute of Technology.

§ Hyperstructured Organic Materials Research Center and School of Materials Science and Engineering, Seoul National University.

⊥ Pohang Accelerator Laboratory.

10.1021/ma070994e CCC: $37.00
Published on Web 08/11/2007

at the same time.[26,27]

We have recently reported interesting crystallization phenomena in nanoscopic cylindrical pores.[28] Crystallization in relatively larger pores was dominated by homogeneous nucleation while heterogeneous nucleation was dominant in smaller pores (pore diameter <50 nm).[28] As our continuing efforts to understand the crystallization of polymers in the cylindrical confinements, we herein report the detailed crystallization and melting and associated crystalline structures (orientation, crystallinity, and size) of PE under nanoscopic cylindrical confinements.

We used fractionated monodisperse linear PE which is a polymeric model material due to its simple chemical structure and well-known properties.[29,30] Monodisperse chain length is expected to minimize the potential effects of the molecular weight distribution and short chain branches on the main chain crystallization.[31] We chose the fractionated linear PE rather than hydrogenated anionically polymerized poly(butadiene) because the 1,2-addition of butadiene monomers cannot be thoroughly avoided.[32]

The anodized nanoporous alumina membranes have several features suitable for examining the crystallization under two-dimensional confinement. The range of the confinement, diameter of the cylindrical nanopore, is quite wide. The dimension is easily controllable in the range of 15−400 nm.[33−36] By using the system with such a wide range of confined dimensions, we could monitor the trend of crystallization behaviors in cylindrical nanopores. Another strong advantage is that the chain ends of the crystalline polymer in the nanopores are free to move. There could be a potential effect of chemical connectivity of one chain end or both ends on the crystallization behavior since the crystallizable chain is chemically tied to other molecules or materials. In addition, the nanoporous alumina provide the robust confinement with excellent thermal and mechanical properties[37] in contrast to the glassy or rubbery matrix in the diblock copolymer systems. Thus, only the effect of the dimensionality of the confinement on the polymer crystallization can be considered since the morphological variation such as the breakout of the matrix in the block copolymer systems is detoured.[16] Besides, the fact that all the nanopores in the anodized alumina are aligned in the direction of alumina membrane thickness would simplify the crystal structure analysis. Overall, the monodisperse linear PE in the nanoporous alumina with a range of diameter is quite ideal to investigate the crystallization and melting behavior of polymer under two-dimensional confinements.

Experimental Section

Materials and Sample Preparation. We purchased a fractionated monodisperse linear PE ($M_w = 32\,100$ g/mol, $M_w/M_n = 1.11$, Standard Reference Material 1483a) from National Institute of Standard and Technology. Alumina membranes with hexagonal arrays of regular-sized cylindrical pores (pore diameter, $D_p = 15-110$ nm) were synthesized via two-step anodization,[38] and a commercial porous alumina membrane (Anodisc 13, $D_p \sim 220$ nm) was purchased from Whatman plc. The morphology of alumina membranes with different pore diameter was characterized by a field-emission scanning electron microscope (FE-SEM, JEOL JSM-6700F, Japan).

To investigate the crystallization behavior of PE in the nanoporous alumina membrane, the linear PE was drawn into the pore via partial wetting or wetting.[39] The linear PE was located selectively in the nanopores. PE and poly(2-vinylpyridine) (P2VP, $M_w \sim 100\,000$ g/mol, Scientific Polymer Products, Inc.) was solution-cast on a glass slide. To eliminate the residual solvents, the films and alumina membranes were dried in a vacuum oven at 185 °C for 2 days. After drying each film, bilayer films composed of a PE top layer and a P2VP bottom layer were prepared by floating PE film on water and then transferring the PE film onto the P2VP-coated slide glass.[40] P2VP film herein acts as a soft supporting layer for the PE film to keep in contact with the alumina membrane during annealing. After placing an alumina membrane on the surfaces of the bilayer films, the assembled samples were annealed in a vacuum oven at 185 °C for 5 days to fill the porous alumina with linear PE (and a small amount of P2VP near the entrance of the pores). The supportive aluminum was eliminated by immersing the samples into the cupric chloride solution.[41] The residual P2VP was removed by immersing in ethanol at 50 °C for about 5 days. We confirmed that no continuous polymer films remained on the surfaces of the alumina templates by observing the sample surfaces with FE-SEM. Additionally, it should be mentioned that the PE material in the nanopores existed in the form of nanorods, not nanotubes, in the nanoporous alumina templates, which was confirmed from TEM images of samples obtained after dissolving the alumina templates (Supporting Information).

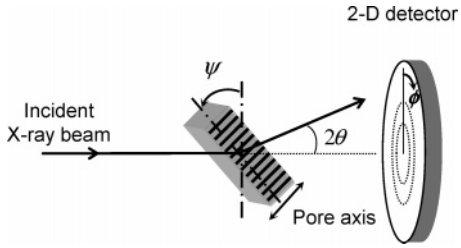

Figure 1. Schematic illustration of the X-ray diffraction geometry employed for investigating the orientation of the PE crystals developed in the cylindrical nanoporous alumina with different pore diameter. The angle ψ was varied from 0° to 89.85° to examine the relationship between the orientation of the PE crystals and the geometry of the nanopores.

X-ray Diffraction. The crystal structure of linear PE in the nanopores was characterized using the X-ray diffraction (XRD) method. Crystallization of the linear PE in the nanopores was conducted by cooling at a rate of 0.5 °C/min from 180 to 30 °C in a vacuum oven. The XRD experiments were carried out by using a synchrotron radiation facility, 4C2 beamline of Pohang Light Source (PLS, Pohang, Republic of Korea, bending magnet type, critical energy: 5.5 keV at 2.5 GeV). X-ray beams of $\lambda = 1.68$ Å were monochromatized by a Si (111) double-crystal monochromator and focused at the sample position in square shape via a toroidal mirror and slits. The beam size at the sample position was 500×500 μm^2. The geometry of XRD experiments is schematically presented in Figure 1. The angle ψ was varied to be 0°, 45°, and 89.85° by a four-circle goniometer. The diffracted patterns were recorded on a 2-D CCD camera (2048×2048 pixel). The sample-to-detector distance was about 15 cm. The diffracted angle was calibrated by powder diffraction of pure silicon which has an intense (111) reflection at $2\theta = 28.44°$.

Melting and Isothermal Crystallization. The melting and isothermal crystallization behaviors of linear PE in the nanoporous alumina were investigated by a Perkin-Elmer DSC7 with a refrigerating cooler. The instrument was calibrated with indium and zinc before experiments. The alumina membranes, filled with linear PE in their nanopores, were placed in aluminum pans. The weight of linear PE in the pan was calculated on the basis of the thickness of PE film and the total area of the membrane disks in the pan. For melting experiments, the samples were heated to 180 °C, held for 10 min to erase the thermal history, cooled to 30 °C, and then heated again to 180 °C. The heating and cooling was controlled at a rate of 10 °C/min. For isothermal crystallization experiments, the samples were heated to 180 °C, held for 10 min, then cooled at a rate of 100 °C/min to each crystallization temperature (T_c). The crystallization exotherm at a given crystallization temperature was monitored as a function of time.

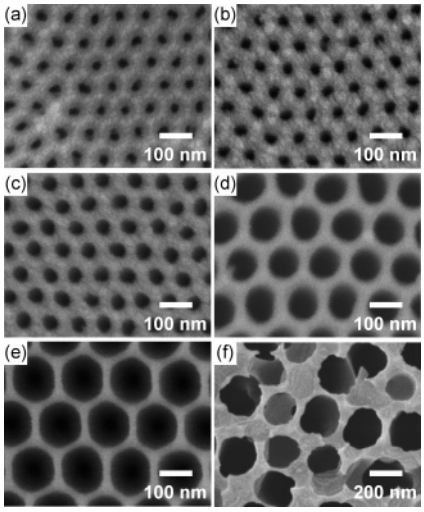

Figure 2. FE-SEM images of nanoporous alumina membranes with a variety of average pore diameter: (a) 15, (b) 20, (c) 30, (d) 62, (e) 110, and (f) 220 nm.

Results and Discussion

FE-SEM images indicate that the fabricated alumina membranes in this study have regular-sized nanopores with mean pore diameters of 15, 20, 30, 62, and 110 nm, as shown in Figure 2a−e. The nanopores were also found to have narrow size distributions. The standard deviations of pore diameters were analyzed to be 1.9, 1.9, 2.0, 2.1, and 3.3 nm, respectively. In contrast, the commercially available membrane (Figure 2f) has the mean pore diameter of 220 nm and a very broad pore size distribution with the standard deviation of ∼46 nm. The pore length (l_p) for all the homemade membranes was around 100 μm.

Isothermal Crystallization Kinetics. DSC thermograms recorded during the isothermal crystallization of linear PE in the nanocylinders of 15 and 110 nm in diameter and in the bulk are representatively shown in Figure 3a−c. The PE in the nanopores and in the bulk exhibited different crystallization behavior especially at the initial stage of the isothermal crystallization. As shown in Figure 3d, nearly linear developments of crystallinity were observed for the crystallization of PE in the nanopores. In contrast, an induction period was observed for the crystallization of PE in bulk.

The Avrami theory was applied to characterize the influence of the 2-D confinement on the crystallization kinetics of PE. The Avrami equation that describes the crystallization kinetics of materials is expressed as[42]

$$1 - X_{c,r} = \exp(-Kt^n)$$

where $X_{c,r}$ is the crystallinity normalized by the finally reached value (i.e., relative crystallinity). The prefactor K and the exponent n are referred to as Avrami constants. K is the constant depicting the contribution of the growth rate, the nucleation rate, and the number of nucleus. The exponent n depends on the growth geometry and the mechanism of the nucleation.

Figure 4 shows Avrami plots obtained from the isothermal crystallization thermograms. The Avrami exponents were evaluated by linear fitting of the initial part of each curve in Figure 4. The n values of linear PE crystallized in the nanopores, 1.6−1.9, were smaller than the one obtained from the bulk crystallization, $n \sim 2.4$. As the pore diameter decreased, the n value decreased to 1.5. These smaller n values are comparable to the ones observed in other confined semicrystalline polymer systems such as the crystallization within the discrete microdomains of block copolymers.[14−16] Because of the geometrical constraints, the nucleation became dominant rather than the growth of the crystallites in the nanoscopic confinement, and therefore the crystallization of the polymers under such constrained geometries followed the first-order kinetics. In the previous study, we found that the crystallization of linear PE in the nanoporous alumina occurred much lower temperatures than in bulk.[28] While one-dimensional growth of the crystals could result in the reduced n values,[42] the low temperature of crystallization that we have observed previously is another important indication of dominant nucleation.[43] In this study, the perfect first-order kinetics was not observed. It is thought that the overall crystallization of PE in the cylindrical nanopores is dominated by the nucleation and the limited crystal growth can still occur along the unconstrained cylindrical axis direction. Even for 220 nm nanopores, the largest pore diameter in this study, the Avrami exponent ($n = 1.8$) is much smaller than that of the bulk ($n = 2.4$), indicating that the crystallization within the nanocylinders of those dimensions is still different from the bulk crystallization. It is understandable by considering that the size of bulk PE spherulite, typically ranging from several micrometers to tens of micrometer, is still much larger than the pore diameter. The rate constants of isothermal crystallization, K, were obtained from the intercepts of each plot in Figure 4. The K values for the crystallization of PE in the nanopores were much larger (more than 5 orders of magnitude) than the one in the bulk.[28] This seems to be originated from the larger number of nuclei in the nanopores.

Crystal Orientation. Figure 5 shows the XRD patterns acquired at referred ψ angles for linear PE in the nanopores with different diameter. Apparently, the diffraction peaks become intense as the pore diameter increases. For instance, the peak intensity from the sample with 110 nm pore was twice

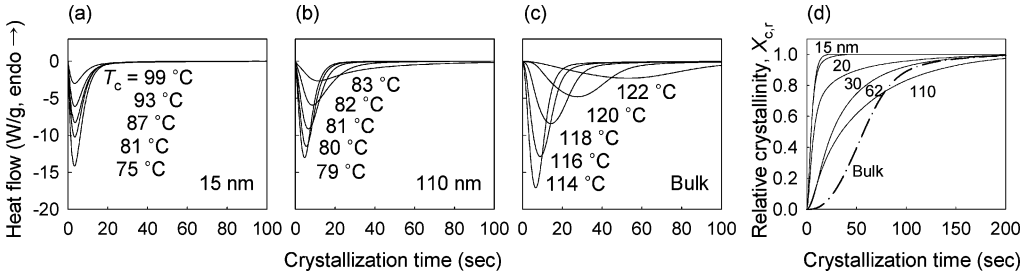

Figure 3. Isothermal crystallization exotherms at various crystallization temperatures for linear PE in the nanoporous alumina with pore diameters of (a) 15 and (b) 110 nm, and (c) in the bulk. (d) is the development of relative crystallinity during isothermal crystallization of linear PE in nanopores (solid lines) and in the bulk (dash−dot line). The crystallization temperatures were 99 °C (15 nm), 93 °C (20 nm), 99 °C (30 nm), 82 °C (62 nm), 83 °C (110 nm), and 122 °C (bulk).

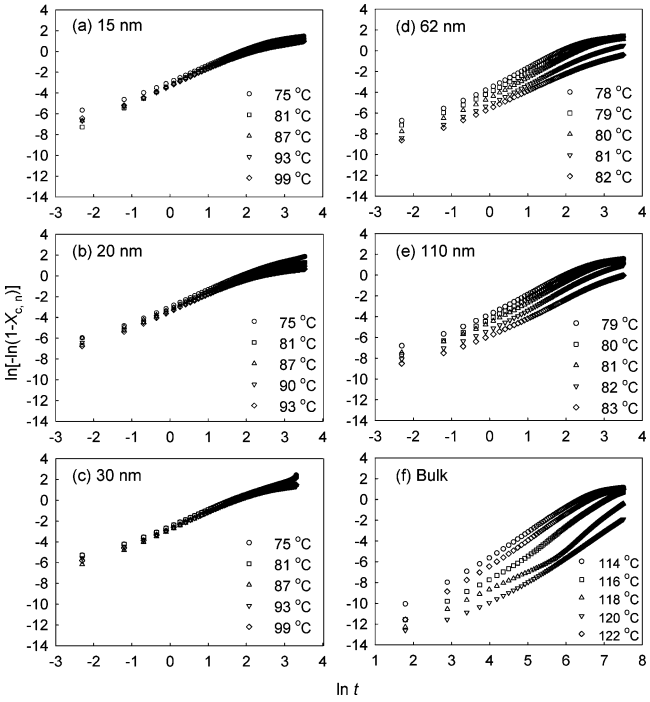

Figure 4. Avrami plots of isothermal crystallization of linear PE in the nanoporous alumina with different pore diameter.

larger than that from 15 nm after the normalization with the amount of linear PE in the nanopores. It is believed that the intensity difference between samples originates from their crystallinity difference. This will be discussed in more detail at the following section.

The XRD patterns at $\psi = 0°$ (the first row of Figure 5) were obtained from the samples where the long axes of the cylindrical nanopores were aligned parallel to the incident X-ray beam. The patterns show typical diffraction of isotropic orthorhombic PE crystals. The uniform diffraction rings from the center of a pattern are (*hk*0) reflections of (110) and (200) for orthorhombic PE crystals. Higher order reflections were not distinct enough to be analyzed because of their weak intensity and overlap between them. For the diffraction patterns at $\psi = 45°$ (the second row of Figure 5), the orientation of (200) diffraction peaks was observed to align on the directions around $\phi = 80°$. When $\psi = 89.85°$ (the setup is identical as grazing incidence diffraction geometry with an incident angle of 0.15°), (110) reflections were clearly observed in the direction of $\phi \sim 32°$. However, (200) reflections, which were supposed to appear at the equator of $\phi = 90°$, were not observed due to the blockage of the alumina membranes. Overall, it is found from the ψ-dependent X-ray diffraction patterns that the *c*- and *a*-axes of orthorhombic PE crystals are preferentially aligned perpendicular to the long axis of nanopores, while the *b*-axis is parallel to it. The (110) and (200) reflections observed in the diffraction patterns of all the samples indicate that the linear PE crystals developed in the nanopores have similar orientation. Figure 6 shows the schematic illustration of PE crystals developed in nanoporous alumina with the crystallographic axes of orthorhombic PE crystals.

The most common morphological measure of orientation is the Herman's orientation function, *f*.[44] The calculation of *f* is meaningful only when there is a maximum of azimuthal intensity distribution at the same or perpendicular direction with the reference direction. However, we could not observe any reflection which has a maximum at the same or perpendicular direction with our reference direction, the cylindrical axis direction. Instead of *f*, we evaluated the full width at half-maximum (FWHM) of the peak in the azimuthal intensity distribution to evaluate the degree of orientation. The normalized azimuthal intensity distribution of (110) reflection observed at $\psi = 89.85°$ and FWHM (inset) as a function of nanopore diameter are shown in Figure 7. The peak at around $\phi = 32°$ was broadened with the increment of pore diameter as can be seen clearly by the decrement of FWHM. The result supports that the degree of orientation decreases with increasing the pore diameter. It demonstrates that the effect of the confinement on the polymer crystallization becomes weaker as the pore gets larger.

The preferred orientation of orthorhombic PE crystals in the nanopore is understandable by considering the kinetically preferred nucleation and crystal growth. In the bulk, for the PE nuclei formed along the preferential direction, the crystal growth occurs along both ⟨110⟩ and ⟨100⟩ directions.[45,46] The ratio of the two linear growth rates, G_{110}/G_{100}, increases with increasing crystallization temperature, and it becomes always greater than unity at T_cs above 80 °C.[46] In other words, the PE crystals grow faster along the ⟨110⟩ direction than ⟨100⟩ direction at higher T_cs, and therefore the PE crystals "elongated along the *b*-axis" are formed at T_cs above 80 °C. As mentioned above, we prepared the samples at a cooling rate of 0.5 °C/min from 180

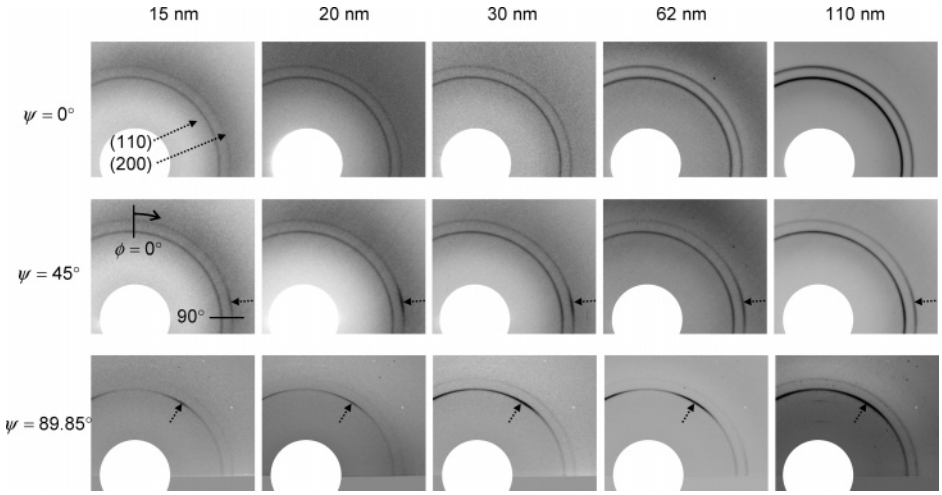

Figure 5. X-ray diffraction patterns at tilt angles of $\psi = 0°$, 45°, and 89.85° for linear PE, crystallized at a cooling rate of 0.5 °C/min, in nanoporous alumina with pore diameters of 15, 20, 30, 62, and 110 nm.

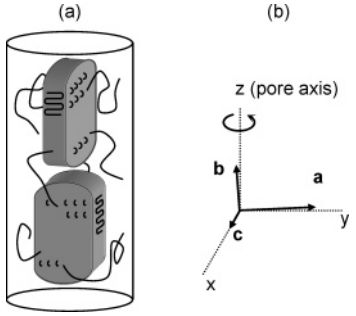

Figure 6. (a) Schematic illustration of the PE crystallites developed in the cylindrical nanopores. (b) Correlation between crystallographic axes (*a*, *b*, *c*) of orthorhombic PE crystals and the orthogonal axes (*x*, *y*, *z*) of cylindrical nanopores. The *z*-axis is the long axis of a cylindrical nanopore.

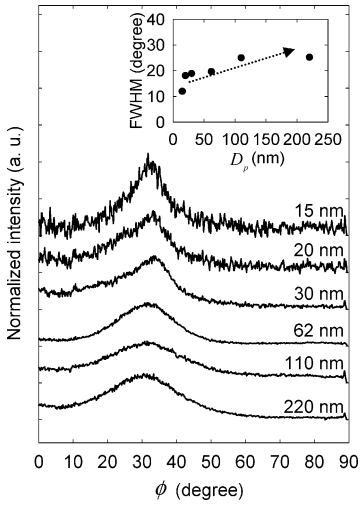

Figure 7. Azimuthal intensity distribution of (110) reflection in X-ray diffraction patterns obtained at the tilt angle of $\psi = 89.85°$. The inset is the plot of the full width at half-maximum (FWHM) of (110) reflection as a function of nanopore diameter.

to 40 °C. In the nanopores, the PE crystallites are expected to develop preferentially along the ⟨110⟩ direction and form elongated shapes along the *b*-axis at the slow cooling. As a result of the cylindrical geometric constraints, the *b*-axis of PE crystal is oriented almost parallel to the long axis of cylindrical nanopores. It has been also reported that, for PVDF crystals developed under nanoporous alumina confinement, the crystal orientation is caused by kinetic selection processes during crystal growth.[47] As shown above, we observed that the crystallization of PE in the nanopores is dominated by the nucleation with the partial contribution of crystal growth.[28] Although the dominant nucleation is thought to render the growth of PE crystals along the long axis of cylindrical nanopores restricted, the crystal orientation can still be driven by the cylindrical geometry during the limited crystal growth.

Melting Behaviors. DSC heating thermograms of PE, crystallized at a cooling rate of 10 °C/min, in the nanoporous alumina are shown in Figure 8. The melting temperature, T_m, was here defined as the peak temperature of the melting thermogram. The T_m of PE crystals developed in nanopores was found to decrease from 128.6 to 122.0 °C with decreasing the pore diameter from 220 to 15 nm. We conjecture this melting temperature depression be due to the decrease of a crystallite size and the increase of interfacial area. Assuming a rectangular-shaped crystal, the relationship between the dimensions of the

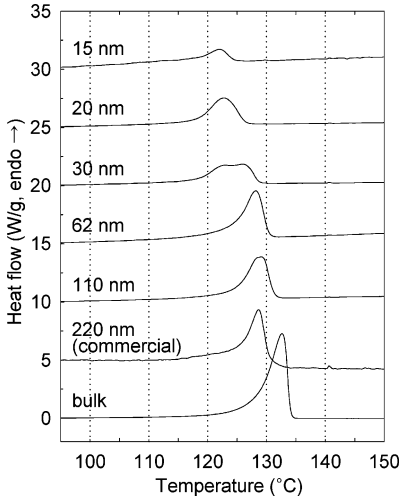

Figure 8. DSC melting thermograms of the linear PE, crystallized at a cooling rate of 10 °C/min, in nanoporous alumina with different pore diameter.

crystal and its melting temperature is well described by the Thomson−Gibbs equation:[48]

$$T_m = T_m^\circ\left[1 - \left(\frac{\sigma_1}{L_1} + \frac{\sigma_2}{L_2} + \frac{\sigma_3}{L_3}\right)\frac{2}{\rho_c \Delta H_m^\circ}\right] \quad (1)$$

where σ_1, σ_2, and σ_3 denotes the specific surface free energy of a crystallites, and L_1, L_2, and L_3 are the dimensions of the crystallite. The subscripts represent the three orthogonal directions in a chain-folded lamella. T_m° is the equilibrium melting temperature of the crystal with infinite thickness, ρ_c is the crystal density, and ΔH_m° is the heat of fusion per unit mass. According to the equation, T_m decreases as the dimension of crystallite (L_1, L_2, and L_3) decreases. In general, the lateral dimensions of the lamellar crystal in bulk are much larger than the thickness. Therefore, the second and third terms in the round bracket of eq 1 are neglected, and the equation is simply represented by the specific free energy of fold surfaces, σ_1 or σ_e, and the thickness of a lamella crystal, L_1 or L_c.

As discussed above, the *c*-axis (the thickness direction of the crystal lamella) of the orthorhombic PE crystals developed in the nanopores is aligned perpendicular to the long axis of cylindrical nanopores. Therefore, one of lateral dimension, normal to pore axis, is restricted. Besides, considering that the overall crystallization in the nanopores is predominated by the nucleation,[28] the lateral dimension of the PE crystals along the pore axis can be also restricted by the growth-limited crystallization. Then, the lateral surface free energies (σ_2 and σ_3) contribute appreciably to lowering the melting temperature of PE, since the lateral surface areas of PE crystals become significant. Additionally, the thickness of PE crystals in nanopores could be reduced, depending on the pore diameter. Eventually, the smaller PE crystals formed in the pore result in the large depression of melting temperature.

For the detailed understanding of crystalline structure and melting behavior, we assume a simple model of PE crystals in the nanopores as follows: (a) linear PE in the nanopores forms rectangular-shaped crystallites with a limited thickness of L_1, where the *c*-axis of orthorhombic PE crystals is oriented perpendicular to the long axis of cylindrical nanopores; (b) L_2-(in the direction of the *a*-axis of crystals) is similar to the pore diameter (D_p). We calculated the melting temperature of this model crystal based on the Thomson−Gibbs equation when L_3 is either infinite or as small as pore diameter. L_3, whose direction

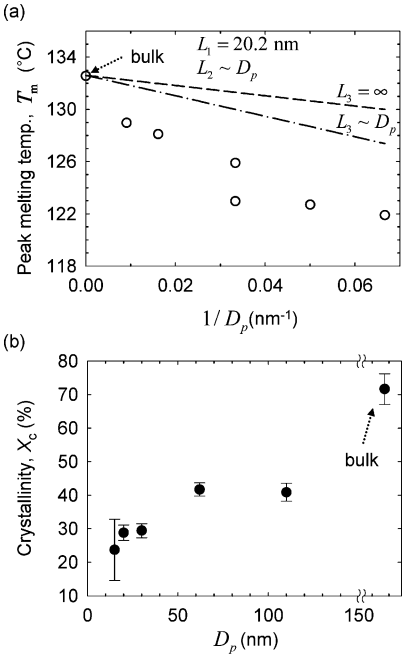

Figure 9. (a) Melting temperature and (b) crystallinity of PE crystals, developed at a cooling rate of 10 °C/min, in nanoporous alumina with different pore diameter. The dashed ($L_1 = 20.2$ nm, $L_2 \sim D_p$, and $L_3 \sim \infty$) and dashed−dot ($L_1 = 20.2$ nm and $L_2 = L_3 \sim D_p$) lines of (a) indicate the melting temperatures calculated from the Thomson−Gibbs equation.

lies parallel to that of pore axis, could be comparable with the pore length in its maximum, assuming perfect crystal growth. In the meantime, L_3 would be very short when the nucleation is dominant in the formation of PE crystal under the cylindrical confinement. Figure 9a shows the experimentally determined melting temperatures of PE crystals in conjunction with the calculated melting temperatures. The dashed line in Figure 9a is drawn with the assumption of $L_1 = 20.2$ nm, $L_2 \sim D_p$, and $L_3 \sim \infty$ and the dash−dot line with $L_1 = 20.2$ nm and $L_2 = L_3 \sim D_p$. L_1 was calculated from the experimentally measured melting temperature of bulk PE using the Thomson−Gibbs equation. The other parameters used for the melting temperature calculations are as follows:[49−51] $T_m^\circ = 419$ K, $\sigma_1 = \sigma_e = 94$ mJ/m^2, $\sigma_2 = \sigma_3 = 13.8$ mJ/m^2, $\rho_c = 1.005$ g/cm^3, and $\Delta H_m^\circ = 293$ J/g. As can be seen in Figure 9a, the melting temperatures calculated with the assumption of $L_3 \sim D_p$ were closer to the experimentally determined melting points than the ones with the assumption of $L_3 \sim \infty$. It supports that the crystal growth along the long axes of the cylindrical nanopores is restricted, and the nucleation is dominant by the nanoscopic confinement. Additionally, we calculated melting temperatures when $L_1 = L_2 = L_3 \sim D_p$. For 15 nm pores, the expected melting point (122.8 °C) was very close to the measured one (121.9 °C), which is also an evidence for the limited crystal growth and nucleation-dominated crystallization in nanopores.

It is noteworthy that the melting temperatures observed experimentally are even lower than the values calculated with the two crystal dimensions assumed above. It implicates that the size of the crystallites developed in nanopores is smaller than the dimensions assumed above. It is known that, for PE crystallite, the fold surface free energy, σ_1 or σ_e, is lager than the other two lateral surface energies, σ_2 and σ_3.[49] We calculated the reduction of crystallite size in the lamella thickness direction, L_1, since it is thought to be a major contribution to the depression of melting temperature. Assuming $L_2 = L_3 \sim D_p$ as before, the L_1s, evaluated from the experimental melting temperatures, were 12.6, 12.7, 12.4, 14.4, 15.7, and 16.2 nm for 15, 20, 30, 62, 110, 220 nm pores, respectively. These L_1s are smaller than the bulk crystal thickness ($L_{c,bulk} = 20.2$ nm) as well as pore diameter, supporting that evaluated L_1 values are reasonable. We performed small-angle X-ray scattering (SAXS) experiments to determine experimentally the L_1 value. But, the L_1 value could not be measured from SAXS patterns because the crystals do not form stacked lamella structure and the scattering signal from the nanopore structure factor is too strong.

In the melting temperature vs reciprocal pore diameter plot (Figure 9a), there is a crossover near 30 nm of pore diameter. Especially, for 30 nm pores, two different melting endothermic peaks were observed (Figure 8). We have recently found that there is a transition of dominant crystallization mechanism of PE in cylindrical nanopores from homogeneous to heterogeneous nucleation as the pore diameter decreased.[28] We believe that the two melting peaks stem from the coexistence of the crystals formed by the two different nucleation mechanism.

The crystallinity (X_c) of linear PE in nanopores was evaluated from the heat of fusion using the following equation:

$$X_c\,(\%) = \frac{\Delta H_m}{\Delta H_m^\circ} \times 100 \qquad (2)$$

where ΔH_m is the heat of fusion measured from the DSC thermogram, and ΔH_m° is the heat of fusion of 100% PE crystal (293 J/g).[51] The evaluated crystallinity as a function of pore diameter is represented in Figure 9b. The crystallinity in the nanopores was found to be less than 50%, which is much smaller than the bulk crystallinity (71.6%). When the pore diameter was smaller than 15 nm, the crystallinity decreased to less than 30%. The result indicates that the crystallization of linear PE was considerably disturbed in the nanopores as the degree of confinement is tightened. The perturbation of crystallization can be attributed to the interference of the cylindrical confinement with the crystal growth, i.e., the limitation of growth by the nanoscopically confined space and the geometrical mismatch between the nanoscopic cylindrical geometry and the crystal growth direction. We could recognize the sharp but minor change in crystallinity with the variation of the pore diameter. While we guess that it is related to the transition of nucleation mechanism,[28] we do not have a concrete picture or experimental clue on the sudden change at the molecular level presently. At least, it is clear that the crystal formation and partial crystal growth in the porous alumina is more perturbed as the pore diameter decreases. Considering that the drop of crystallinity is minor, we believe that the nanoscopically curved geometry of the alumina surface, small space with mechanically solid wall, and the perturbation of chain conformation are more influential on the final crystallinity than the nucleation mechanism transition.

Conclusions

We investigated the crystalline features (orientation, size, crystallinity, etc.), melting, and crystallization of linear PE under the nanoscopic cylindrical confinement. It was found that the frustration driven by the nanoscopic constrained geometry induced the nucleation-dominant crystallization. A specific orientation of linear PE crystals in nanocylinders was found when they were crystallized slowly; the *b*-axis of orthorhombic PE crystals was parallel to the long cylindrical axes of the nanopores, and *a*- and *c*-axes were nearly on the plane perpendicular to the cylindrical axes. The melting temperature of PE crystals developed in the nanopores decreases appreciably

with the decrement of pore diameters due to the reduced crystal size. The crystallinity of linear PE in the nanoporous alumina was also significantly reduced.

Acknowledgment. This work was supported by KRF (MOEHRD, Basic Research Promotion Fund for new faculties, KRF-2006-331-D00160) and KOSEF (Basic Research Program, R01-2006-000-10749-0). Financial support from Seoul National University through the program of supporting new faculty is also gratefully acknowledged. The authors appreciate the experimental support by the staffs at the 4C2 and 8C1 beamline of Pohang Light Source.

Supporting Information Available: TEM images of PE nanorods. This material is available free of charge via the Internet at http://pubs.acs.org.

References and Notes

(1) Keddie, J. L.; Jones, R. A. L.; Cory, R. A. *Europhys. Lett.* **1994**, *27*, 59.
(2) Wallace, W. E.; Van Zanten, J. H.; Wu, W. L. *Phys. Rev. E* **1995**, *52*, R3329.
(3) Forrest, J. A.; Mattsson, J. *Phys. Rev. E* **2000**, *61*, R53.
(4) Zheng, X.; Sauer, B. B.; Vanalsten, J. G.; Schwarz, S. A.; Rafailovich, M. H.; Sokolov, J.; Rubinstein, M. *Phys. Rev. Lett.* **1995**, *74*, 407.
(5) Kim, J. U.; Cha, S. H.; Shin, K.; Jho, J. Y.; Lee, J. C. *Adv. Mater.* **2004**, *16*, 459.
(6) Shin, K.; Xiang, H. Q.; Moon, S. I.; Kim, T.; McCarthy, T. J.; Russell, T. P. *Science* **2004**, *306*, 76.
(7) Frank, C. W.; Rao, V.; Despotopoulou, M. M.; Pease, R. F. W.; Hinsberg, W. D.; Miller, R. D.; Rabolt, J. F. *Science* **1996**, *273*, 912.
(8) Noh, K. W.; Woo, E.; Shin, K. *Chem. Phys. Lett.* **2007**, *444*, 130.
(9) Despotopoulou, M. M.; Miller, R. D.; Rabolt, J. F.; Frank, C. W. *J. Polym. Sci., Part B: Polym. Phys.* **1996**, *34*, 2335.
(10) Despotopoulou, M. M.; Frank, C. W.; Miller, R. D.; Rabolt, J. F. *Macromolecules* **1996**, *29*, 5797.
(11) Hong, S.; MacKnight, W. J.; Russell, T. P.; Gido, S. P. *Macromolecules* **2001**, *34*, 2876.
(12) Chen, H. L.; Wu, J. C.; Lin, T. L.; Lin, J. S. *Macromolecules* **2001**, *34*, 6936.
(13) Cohen, R. E.; Bellare, A.; Drzewinski, M. A. *Macromolecules* **1994**, *27*, 2321.
(14) Loo, Y. L.; Register, R. A.; Ryan, A. J. *Phys. Rev. Lett.* **2000**, *84*, 4120.
(15) Loo, Y. L.; Register, R. A.; Ryan, A. J.; Dee, G. T. *Macromolecules* **2001**, *34*, 8968.
(16) Loo, Y. L.; Register, R. A.; Ryan, A. J. *Macromolecules* **2002**, *35*, 2365.
(17) Zhu, L.; Cheng, S. Z. D.; Calhoun, B. H.; Ge, Q.; Quirk, R. P.; Thomas, E. L.; Hsiao, B. S.; Yeh, F. J.; Lotz, B. *J. Am. Chem. Soc.* **2000**, *122*, 5957.
(18) Huang, P.; Zhu, L.; Guo, Y.; Ge, Q.; Jing, A. J.; Chen, W. Y.; Quirk, R. P.; Cheng, S. Z. D.; Thomas, E. L.; Lotz, B.; Hsiao, B. S.; Avila-Orta, C. A.; Sics, I. *Macromolecules* **2004**, *37*, 3689.
(19) Huang, P.; Zhu, L.; Cheng, S. Z. D.; Ge, Q.; Quirk, R. P.; Thomas, E. L.; Lotz, B.; Hsiao, B. S.; Liu, L. Z.; Yeh, F. J. *Macromolecules* **2001**, *34*, 6649.
(20) Zhu, L.; Calhoun, B. H.; Ge, Q.; Quirk, R. P.; Cheng, S. Z. D.; Thomas, E. L.; Hsiao, B. S.; Yeh, F.; Liu, L. Z.; Lotz, B. *Macromolecules* **2001**, *34*, 1244.
(21) Ogata, N.; Kawakage, S.; Ogihara, T. *Polymer* **1997**, *38*, 5115.
(22) Jiang, S.; Yu, D.; Ji, X.; An, L.; Jiang, B. *Polymer* **2000**, *41*, 2041.
(23) Jiang, S. C.; Ji, X. L.; An, L. J.; Jiang, B. Z. *Polymer* **2001**, *42*, 3901.
(24) Steinhart, M.; Senz, S.; Wehrspohn, R. B.; Gosele, U.; Wendorff, J. H. *Macromolecules* **2003**, *36*, 3646.
(25) Bates, F. S.; Fredrickson, G. H. *Annu. Rev. Phys. Chem.* **1990**, *41*, 525.
(26) Thurn-Albrecht, T.; Schotter, J.; Kastle, C. A.; Emley, N.; Shibauchi, T.; Krusin-Elbaum, L.; Guarini, K.; Black, C. T.; Tuominen, M. T.; Russell, T. P. *Science* **2000**, *290*, 2126.
(27) Shin, K.; Leach, K. A.; Goldbach, J. T.; Kim, D. H.; Jho, J. Y.; Tuominen, M.; Hawker, C. J.; Russell, T. P. *Nano Lett.* **2002**, *2*, 933.
(28) Woo, E.; Huh, J.; Jeong, Y. G.; Shin, K. *Phys. Rev. Lett.* **2007**, *98*, 136103.
(29) Strobl, G. *Eur. Phys. J. E* **2000**, *3*, 165.
(30) Rastogi, S.; Spoelstra, A. B.; Goossens, J. G. P.; Lemstra, P. J. *Macromolecules* **1997**, *30*, 7880.
(31) Rhee, J.; Crist, B. *J. Polym. Sci., Part B: Polym. Phys.* **1994**, *32*, 159.
(32) Balsamo, V.; Muller, A. J.; Stadler, R. *Macromolecules* **1998**, *31*, 7756.
(33) Keller, F.; Hunter, M. S.; Robinson, D. L. *J. Electrochem. Soc.* **1953**, *100*, 411.
(34) Diggle, J. W.; Downie, T. C.; Goulding, C. W. *Chem. Rev.* **1969**, *69*, 365.
(35) Thompson, G. E. *Thin Solid Films* **1997**, *297*, 192.
(36) Li, A. P.; Muller, F.; Birner, A.; Nielsch, K.; Gosele, U. *J. Appl. Phys.* **1998**, *84*, 6023.
(37) Alcala, G.; Mato, S.; Skeldon, P.; Thompson, G. E.; Mann, A. B.; Habazaki, H.; Shimizu, K. *Surf. Coat. Technol.* **2003**, *173*, 293.
(38) Masuda, H.; Fukuda, K. *Science* **1995**, *268*, 1466.
(39) Steinhart, M.; Wehrspohn, R. B.; Gosele, U.; Wendorff, J. H. *Angew. Chem., Int. Ed.* **2004**, *43*, 1334.
(40) Forrest, J. A.; DalnokiVeress, K.; Dutcher, J. R. *Phys. Rev. E* **1997**, *56*, 5705.
(41) Sun, Y. M.; Steinhart, M.; Zschech, D.; Adhikari, R.; Michler, G. H.; Gosele, U. *Macromol. Rapid Commun.* **2005**, *26*, 369.
(42) Avrami, M. *J. Chem. Phys.* **1939**, *7*, 1103.
(43) Reiter, G.; Castelein, G.; Sommer, J. U.; Rottele, A.; Thurn-Albrecht, T. *Phys. Rev. Lett.* **2001**, *87*, 226101.
(44) Gedde, U. W. *Polymer Physics;* Chapman & Hall: London, 1995; p 201.
(45) Organ, S. J.; Keller, A. *J. Polym. Sci., Part B: Polym. Phys.* **1986**, *24*, 2319.
(46) Gedde, U. W. *Polymer Physics;* Chapman & Hall: London, 1995; p 138.
(47) Steinhart, M.; Goring, P.; Dernaika, H.; Prabhukaran, M.; Gosele, U.; Hempel, E.; Thurn-Albrecht, T. *Phys. Rev. Lett.* **2006**, *97*, 027801.
(48) Gedde, U. W. *Polymer Physics;* Chapman & Hall: London, 1995; p 144.
(49) Hoffman, J. D.; Frolen, L. J.; Ross, G. S.; Lauritzen, J. I. *J. Res. Natl. Bur. Stand., Sect. A: Phys. Chem.* **1975**, *79*, 671.
(50) Wunderlich, B. *Macromolecular Physics;* Academic Press: New York, 1973; Vol. 2, p 25.
(51) Wunderlich, B. *Macromolecular Physics;* Academic Press: New York, 1973; Vol. 3, p 39.

MA070994E